Chapter 6
Biomolecules, Photostability and $^1\pi\sigma^*$ States: Linking These with Femtochemistry

Gareth M. Roberts and Vasilios G. Stavros

Abstract In an effort to illuminate why nature has chosen a particular set of bio-molecular 'building-blocks' for life, a surge of gas phase experiments have recently targeted understanding why key DNA bases, amino acids and their corresponding chromophore subunits, exhibit a resistance to photochemical damage (photostability) following ultraviolet radiation absorption. The research considered in this chapter focuses on the role of dissociative $^1\pi\sigma^*$ states in photostable behavior, and in particular H-atom elimination mediated *via* these states. By probing the timescales for the appearance of these H-atoms using ultrafast lasers coupled to molecular beam methodologies, important information pertaining to the excited state dynamics of these molecules can be obtained. We also discuss how the information gleaned from these studies can be used as a 'stepping-stone' for extending this research to larger, more complex biomolecules and, ultimately, more realistic systems in solution.

6.1 Introduction

Over the years a vast arena of interdisciplinary research has strived to understand the important characteristics of many biomolecules at a molecular level. Recently though, the contemporary discipline of ultrafast biophysics has led to a number of important breakthroughs regarding our understanding of key biological processes. This has been achieved by probing the excited electronic (and vibrational) state dynamics involved in these, often complex, natural systems [1]. Whilst this is not intended to be an exhaustive list, this field has aided in intimately mapping the trigger mechanism for human vision in rhodopsin [2, 3], efficient light harvesting processes occurring within photosynthesis [4] and the origins of high fluorescence quantum yields in numerous fluorescent protein variants [5, 6]. Such feats truly emphasize how probing the excited state dynamics of biological species on an ultrafast

G.M. Roberts · V.G. Stavros (✉)
Department of Chemistry, University of Warwick, Library Road, Coventry CV4 7AL, UK
e-mail: v.stavros@warwick.ac.uk

G.M. Roberts
e-mail: g.m.roberts@warwick.ac.uk

timescale can provide unparalleled insights into the mechanisms underpinning a diverse range of fundamental processes in biology.

The examples mentioned above highlight how light induced biochemistry can be essential for life. In contrast though, light's interaction with living organisms can also be highly detrimental. In particular, following photoexcitation with ultraviolet (UV) radiation, the electronically excited states of UV chromophores in DNA (DNA bases) can potentially trigger ultrafast structural changes (termed photolesions), which modify or terminate its genetic function [7]. These UV triggered processes can often be the fundamental precursors to mutagenesis, carcinogenesis and apoptosis [8]. Through evolution, nature has developed methods to combat these potentially devastating UV induced photoreactions. Light triggered photolyase enzymes, for example, act as one of the final bastions of defense against UV photodamage, by actively repairing photolesion sites in DNA [9]. Fortunately, many of the molecular building-blocks nature has selected for life, particularly the DNA bases, exhibit a built-in resistance against UV triggered damage. For this reason, they are commonly classed as *photostable* species. This photostable behavior is postulated to act as one of the front-line defenses against photodamage, and is so efficient that less than 1 % of UV induced excitation processes in DNA result in the formation of photolesions [10]. Their photostability is believed to be intimately linked to how efficiently electronically excited states can undergo non-radiative relaxation back to the electronic ground state, transforming electronic energy into less harmful thermal (vibrational) energy, which can be dissipated into surrounding solvent. It is this concept of photostability, and the role that specific excited electronic states play in this behavior, which we explore further in this chapter.

6.2 Excited Electronic States and Photostability

With the themes discussed in Sect. 6.1 in mind, a large interest towards understanding the intrinsic photostability of isolated DNA bases and, more generally, molecular subunits of biomolecules (specifically UV chromophores of the DNA bases and amino acids) has ensued. The ultimate vision of this work has been to link photostability to electronic structure. Excited electronic states, by and large, are much more reactive than the ground state and proficiency for rapidly diffusing this harmful energy will invariably aid the photostability of the molecule. Over the last decade, a multitude of studies have been carried out to elicit the details of photochemical pathways that can facilitate photostable behavior. A full description of the numerous reaction pathways that have been identified to date is beyond the scope of this chapter and for further comprehensive discussion the reader is referred to references [10–13] (and references therein).

This chapter discusses the role of $^1\pi\sigma^*$ states in the excited state dynamics of heteroaromatic biomolecules and their UV chromophore subunits. In the seminal theoretical work by Sobolewski *et al.* [14], the potential role of $^1\pi\sigma^*$ states in photostability was postulated through *ab initio* electronic structure calculations. These
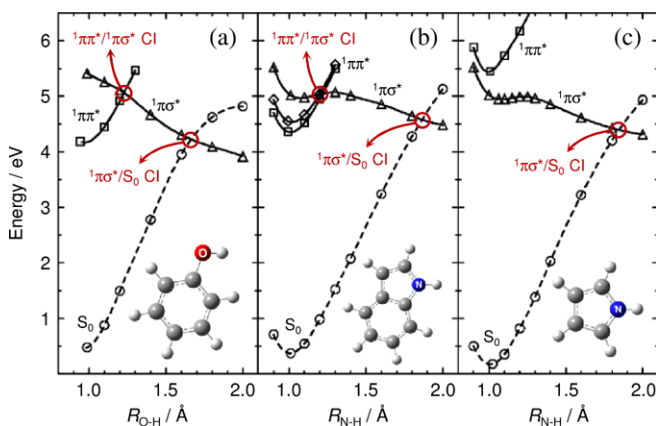
Fig. 6.1 Potential energy cuts of the S_0 ground state and lowest lying $^1\pi\pi^*$ and $^1\pi\sigma^*$ excited electronic states in (**a**) phenol, (**b**) indole and (**c**) pyrrole, as a function of the X–H stretch coordinate (R_{X-H}, where X = O or N). Conical intersections (CIs) are also highlighted. Figure adapted from [14]

studies indicated that $^1\pi\sigma^*$ states may offer a very simple radiationless decay pathway that contributes to the low fluorescence quantum yields observed in many heteroaromatic chromophores (beyond certain excitation energy thresholds).

Figure 6.1 depicts calculated potential energy profiles for (a) phenol, (b) indole and (c) pyrrole [14]—subunits found in tyrosine, tryptophan and hemes, respectively. With reference to these profiles, UV photon energy can be deposited into the molecule through excitation to a strongly absorbing $^1\pi\pi^*$ electronic state (formed as a result of a $\pi^* \leftarrow \pi$ transition). These molecules also possess a weakly absorbing excited electronic state of $^1\pi\sigma^*$ character, which intersects both the $^1\pi\pi^*$ state (phenol and indole, Fig. 6.1(a) and (b), respectively) and the electronic ground state (S_0), forming conical intersections (CIs) along an X–H bond coordinate, where X is typically O or N (see references [15–17] for a rigorous discussion of CIs). Sobolewski *et al*. [14] predicted that, following excitation to the $^1\pi\pi^*$ state and coupling onto the $^1\pi\sigma^*$ state (*via* a $^1\pi\pi^*/^1\pi\sigma^*$ CI), non-radiative decay along this pathway would be highly efficient due to the repulsive nature of this state, leading to either H-atom elimination or efficient relaxation to S_0 *via* a $^1\pi\sigma^*/S_0$ CI. Alternatively, it has also been demonstrated that direct excitation to the weakly absorbing $^1\pi\sigma^*$ state may also occur, leading to analogous behavior [18].

6.2.1 H-Atom Elimination Dynamics Mediated by $^1\pi\sigma^*$ States

Following the absorption of a UV photon, probing H-atom elimination from biomolecules and their subunits provides a very simple means of identifying, in part, the participation of $^1\pi\sigma^*$ states in their excited state dynamics, given that
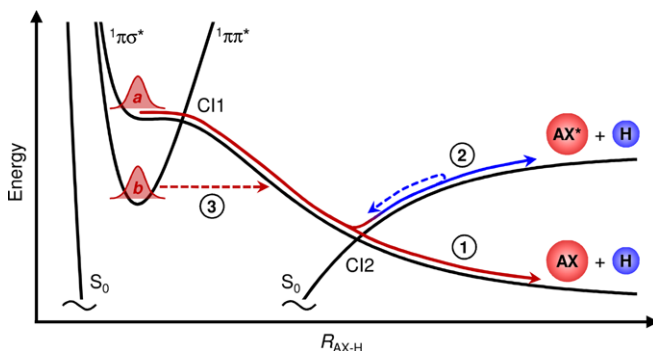
Fig. 6.2 Schematic potential energy cuts (*black*) along an AX–H bond coordinate ($R_{AX–H}$), depicting (1) non-adiabatic, (2) adiabatic and (3) tunneling dynamics, respectively. The details of each process are discussed in the main text. Conical intersections are labeled CI1 and CI2

these states are dissociative along X–H bond coordinates. This approach does require caution though: (i) this method is unable to provide quantitative information regarding the fraction of initially excited molecules which re-access the S_0 ground state through the $^1\pi\sigma^*/S_0$ CI; and (ii) the appearance of H-atoms is not solely indicative of $^1\pi\sigma^*$ mediated dynamics, as a range of processes, including multiphoton dissociative ionization [19, 20] and fragmentation of superexcited states [21], can also lead to the appearance of H-atoms. It is important to acknowledge that the former is currently a non-trivial issue to resolve. However, the latter can be addressed by measuring the kinetic energy (KE) of the H-atoms following photodissociation, or more commonly the total kinetic energy release (TKER). One is then able to correlate particular signatures in the TKER spectrum to H-atom elimination mediated through $^1\pi\sigma^*$ states (see Sect. 6.3.2). This was demonstrated in the pioneering work of Blank *et al*. [22] and later by Wei *et al*. [23].

6.2.2 Non-adiabatic, Adiabatic and Tunneling dynamics

H-atom elimination dynamics along $^1\pi\sigma^*$ states may involve a number of different photophysical processes. Of specific importance here are *non-adiabatic*, *adiabatic* and *tunneling* dynamics. We subsequently introduce these processes with reference to the schematic in Fig. 6.2, which depicts generic potential energy cuts along an AX–H bond, where X = a heteroatom and A = an aromatic moiety.

We begin by considering non-adiabatic behavior. With reference to wavepacket *a* in Fig. 6.2, this photo-prepared flux on the $^1\pi\pi^*$ state may pass through CI1 and proceed towards CI2 along the $^1\pi\sigma^*$ surface. Once at CI2, it can traverse through this CI non-adiabatically (process 1, solid red arrow) leading to direct AX–H bond fission, yielding H-atoms with large amounts of KE in coincidence with AX radical co-fragments. Non-adiabatic dynamics of this kind are typically characterized

by ultrafast dissociation timescales of < 100 fs (see for example [20]). Alternatively, dissociating flux can evolve adiabatically around CI2 (process 2, solid blue arrow), and generate AX radicals in an electronically excited state, AX*, together with H [19, 24]. However, in scenarios where the dissociative flux does not have enough energy to access the higher energy dissociation asymptote (*e.g.* initial photopreparation of wavepacket *b* in Fig. 6.2), some fraction may return towards CI2 (dashed blue arrow) and non-adiabatically couple back onto S_0, forming thermally (vibrationally) hot S_0 molecules [25]. In the gas phase, these vibrationally hot S_0 species may ultimately undergo *statistical unimolecular dissociation* to generate H-atoms with low amounts of KE on a timescale as fast as picoseconds [25, 26].

A third scenario that can occur involves excited state flux tunneling through an energy barrier to access the $^1\pi\sigma^*$ surface (see for example [27–29]). Wavepacket *b* in Fig. 6.2 correlates to flux which has been photo-prepared on $^1\pi\pi^*$ below the energy of CI1. Depending on the size of the barrier area under CI1, the wave-like nature of the flux (in this instance the dissociating H-atom) may enable tunneling under CI1 (process 3, dashed red arrow) and coupling onto the $^1\pi\sigma^*$ state at extended AX–H distances (H tunneling is revisited in Sect. 6.4.3). Timescales for H-atom elimination dynamics mediated through tunneling are inherently linked to the size of the barrier and can range up to nanoseconds [29], but none-the-less, still generate high KE H-atoms as a result of subsequent dissociation on the $^1\pi\sigma^*$ surface.

In the following section we introduce experimental techniques which have been used to identify the participation of these processes in $^1\pi\sigma^*$ based dynamics, with particular focus on methods which monitor the appearance of H-atom photoproducts.

6.3 Experimental Detection of $^1\pi\sigma^*$ Mediated Dynamics

A number of spectroscopic techniques in the gas phase have been utilized to characterize $^1\pi\sigma^*$ mediated dynamics in heteroaromatic chromophores, from both a frequency- and time-domain perspective. Frequency-domain measurements can offer precise information regarding the energetics of the dissociation process and the vibrational motions involved, while time-domain measurements are often able to observe direct participation of these states and their ultrafast temporal evolution. The complementary information yielded from both domains has proved highly fruitful in understanding the role of $^1\pi\sigma^*$ states in the excited state dynamics of a broad range of biomolecules and their subunits (see for example [18, 20, 27, 29–33]). Whilst this chapter focuses on time-domain experiments, we briefly list both approaches for completeness. High resolution frequency-resolved studies have been dominated by photofragment translational spectroscopies, in particular multi-mass ion imaging [34, 35], H (Rydberg) atom photofragment translational spectroscopy [18, 36] and velocity map ion imaging [23, 37]. Time-resolved techniques have included time-resolved photoelectron spectroscopy [31, 38, 39], time-resolved mass spectrometry (TR-MS) [25, 27, 40, 41] and time-resolved velocity map ion imaging (TR-VMI)
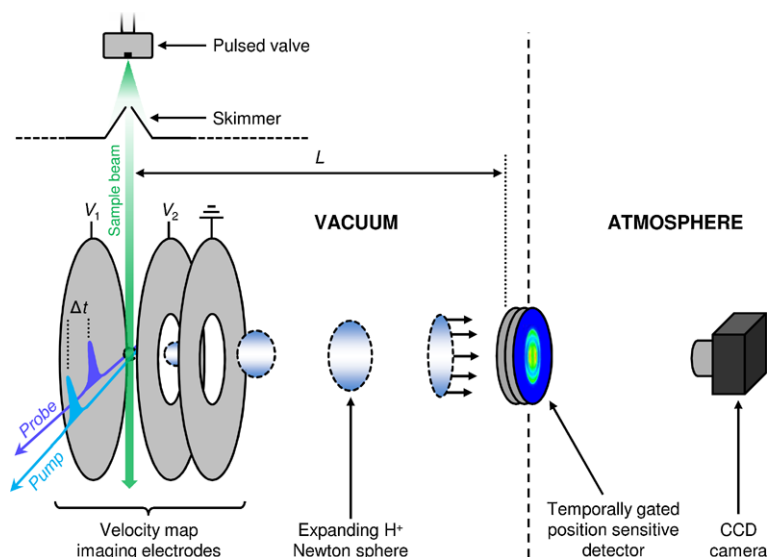
Fig. 6.3 Schematic arrangement of an ultrafast TR-VMI experiment. Further details of the TR-VMI apparatus are discussed in the main text

[20, 26, 29]. In the following sections we specifically describe the use of TR-MS and TR-VMI for probing H-atom elimination mediated by $^1\pi\sigma^*$ states in greater detail.

6.3.1 Time-Resolved Time-of-Flight Mass Spectrometry

TR-MS methods commonly utilize time-of-flight mass-spectrometers (TOF-MS). In these experiments, a skimmed molecular beam of target molecules is produced by seeding a vapor pressure of analyte into a carrier gas (*e.g.* He or Ar), which is admitted into vacuum using a pulsed valve, typically piezoelectrically [42] or solenoid [43] driven. The molecular beam pulse is intercepted perpendicularly by fs laser pulses at the centre of the TOF optics, which usually replicate the arrangement described by Wiley and McLaren [44]—such an electrode arrangement is shown in Fig. 6.3. By applying high voltages (on the order of kVs) to the TOF optics (V_1 and V_2 in Fig. 6.3), ionized photofragments are accelerated into a drift tube, with the same KE, along the time-of-flight axis, L. Whilst the KEs of the ions are the same, their velocities along the flight axis depend on mass. As a result, ions with the lightest mass arrive at the terminus of the flight tube first, followed later by heavier ions. A mass spectrum of ions, resolved by their different time-of-flights, is then collected by a detector placed at the end of the flight tube (which registers ion counts as a function of flight time). The most common type of detector is based around a

microchannel plate (MCP) assembly, which possesses very high ion detection sensitivity (> 80 % [45]).

With regards to probing the timescales for H-atom elimination, a fs pump pulse photoexcites the molecules of interest, defining the zero of time ($\Delta t = 0$) for the experiment, while a time delayed fs probe pulse, centered at 243 nm, ionizes any H-atom photoproducts through $(2 + 1)$ resonance enhanced multiphoton ionization (REMPI), generating H^+. Both fs pump and probe pulses are typically derived from optical parametric amplifiers (OPAs) [46], commonly seeded by the output of a commercial ultrafast Ti:sapphire laser system. All ions, including H^+, are then analyzed using TOF-MS. By recording a mass spectrum at a series of different time delays (Δt) between the fs pump and probe pulses, and integrating only the H^+ counts in the mass spectrum at each Δt, the buildup of H^+ can be tracked in real time. The generated H^+ signal transient can then be modeled using appropriate functions (*e.g.* an exponential rise function convoluted with the temporal instrument response function—see Sect. 6.4.1) to obtain a time-constant, τ, for the appearance of H-atoms. However, as discussed in Sect. 6.2.1, the mere detection of H-atoms is not necessarily indicative of $^1\pi\sigma^*$ mediated dynamics. A more complete picture of $^1\pi\sigma^*$ mediated H-atom elimination can be attained using time-resolved photofragment translational spectroscopies, such as TR-VMI, which can monitor both the ultrafast appearance timescales and KEs of any H photoproducts.

6.3.2 Time-Resolved Velocity Map Ion Imaging

Charged particle imaging techniques [47] and, in particular, velocity map ion imaging (VMI) [37], have revolutionized the field of photofragment spectroscopy and are now essential methodologies used in gas phase molecular reaction dynamics [48]. One of the major advantages of VMI is that it simultaneously recovers both the recoil speed and the angular recoil trajectories (velocity vectors) of the original 3-D distribution of ionized photofragments (Newton sphere) by collecting its 2-D projection. With respect to the schematic in Fig. 6.3, VMI is typically implemented using a *gridless* Wiley-McLaren TOF electrode arrangement, which both temporally and spatially focus ions onto a *position sensitive* detector (typically a pair of MCPs coupled to a phosphor screen) placed at the terminus of a field-free flight tube. By temporally gating the detector, it is possible to collect the 2-D projection of only a specific photofragment mass of interest, m_f, based on its known TOF, t, to the detector, given by:

$$t = L\sqrt{\frac{m_f}{2eV_1}} \tag{6.1}$$

where V_1 is the voltage on the accelerator plate of the VMI arrangement, e is the elementary charge and L is the distance from the laser-molecule interaction point to the front plane of the detector. Unlike the gridded electrodes used in a standard Wiley-McLaren TOF-MS, the gridless electrodes used in VMI lead to the

formation of an electrostatic lens, which causes ionized photofragments with the same velocity vectors to be focused onto the same position of the 2-D detector plane, regardless of their initial position within the ionization volume of the focused probe laser. As a result, carefully designed VMI arrangements, in combination with high-resolution frequency-domain studies, can deliver an energy resolution down to $\Delta E/E = 0.38\ \%$ [49]. Although this energy resolution is not achievable in ultrafast TR-VMI experiments, due to the inherently broad bandwidth of fs pulses (typically hundreds of cm^{-1}), coupling ultrafast pump-probe spectroscopy with VMI still vitally affords temporal and energy information (as well as photofragment angular recoil information—*vide infra*), regarding photodissociation mechanisms, unlike TR-MS. For completeness, we highlight that, very recently, magnetic-bottle analyzers (which are traditionally used to perform photoelectron spectroscopy [38]) have been adapted to perform time-resolved photofragment translational spectroscopy measurements on H^+ [50, 51], also delivering energy and time information about $^1\pi\sigma^*$ dynamics.

At each pump-probe time delay, Δt, the desired 1-D TKER distribution can be recovered from a measured 2-D H^+ velocity map image using image reconstruction methods [52–54]. Reconstruction algorithms return the 1-D radial (r) spectrum, which may then be converted into KE space using an appropriate Jacobian ($r^2 \propto$ KE) and a KE calibration factor. The latter is obtained by measuring photofragments from a well characterized dissociation event (*e.g.* ionizing H-atoms from photolyzed HBr [55]). The measured KE of the photofragments may finally be converted into the desired TKER scale according to:

$$\text{TKER} = \text{KE}\left(\frac{m_\text{p}}{m_\text{p} - m_\text{f}}\right) \tag{6.2}$$

where m_p is the mass of the parent molecule.

When considering $^1\pi\sigma^*$ mediated H-atom elimination dynamics, the different signal features in the derived TKER distribution can be related back to different photodissociation mechanisms. We consider this with respect to the schematic potentials in Fig. 6.4(a). Dynamics proceeding along dissociative $^1\pi\sigma^*$ states typically generate features with large TKERs [18]. For a parent species, AX–H, in its zero point vibrational level prior to photoexcitation, partitioning of the available energy into TKER during this dissociation process can be understood according to:

$$\text{TKER} = h\nu_\text{pu} - D_0(\text{AX–H}) - E_\text{elec} - E_\text{vib} \tag{6.3}$$

where $h\nu_\text{pu}$ is the pump photon energy, $D_0(\text{AX–H})$ is the AX–H bond strength, and E_elec and E_vib are the electronic and vibrational energies of the radical co-fragments, AX. The maximum TKER, TKER_max, after AX–H dissociation along the $^1\pi\sigma^*$ surface corresponds to a scenario where radical co-fragments are formed with zero internal energy ($E_\text{elec} = 0$ and $E_\text{vib} = 0$), following non-adiabatic dynamics through the $^1\pi\sigma^*/S_0$ CI. In this case, Eq. (6.3) simplifies to:

$$\text{TKER}_\text{max} = h\nu_\text{pu} - D_0(\text{AX–H}) \tag{6.4}$$
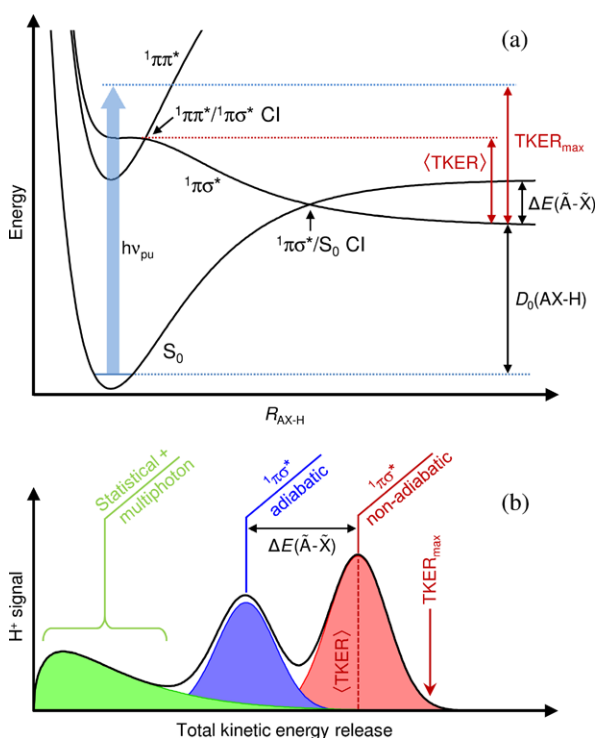
In TR-VMI studies, features associated with $^1\pi\sigma^*$ mediated AX–H fission, evolving non-adiabatically around the $^1\pi\sigma^*/S_0$ CI, typically appear as Gaussian-like profiles at high TKERs (Fig. 6.4(b), red shading). Depending on the initial $h\nu_{\text{pu}}$ energy and the energy partitioning between TKER and E_{vib}, the high energy 'tail' of these features may extend to (approximately) TKER$_{\text{max}}$ [56, 57]. As illustrated by Fig. 6.4(b), the central (mean) TKER of the non-adiabatic $^1\pi\sigma^*$ feature, $\langle$TKER$\rangle$, is related to the energy difference between the plateau region of the $^1\pi\sigma^*$ surface (caused by an avoided crossing between the $^1\pi\sigma^*$ valence state and a $^1\pi3s$ Rydberg state near the vertical Franck-Condon region [18, 58]) and the dissociation asymptote—note that an alternative interpretation of $\langle$TKER$\rangle$ is required for tunneling dynamics under a $^1\pi\pi^*/^1\pi\sigma^*$ CI, as discussed in Sect. 6.4.3. Equation (6.3) also highlights that it is possible, in principle, to distinguish between non-adiabatic and adiabatic dynamics around the $^1\pi\sigma^*/S_0$ CI—the latter generates electronically excited AX co-fragments ($E_{\text{elec}} = \Delta E(\tilde{A} - \tilde{X})$), giving rise to a Gaussian-like feature which is red-shifted in TKER, relative to the location of the non-adiabatic feature, by $\Delta E(\tilde{A} - \tilde{X})$ (Fig. 6.4(b), blue shading). Similarly, H$^+$ signals originating from multiphoton processes and statistical unimolecular dissociation of vibrationally hot S_0 species peak at low TKERs and typically exhibit broad signal profiles peaked at low TKER (Fig. 6.4(b), green shading) [18, 26, 59, 60], allowing them to be readily distinguished from direct AX–H fission along $^1\pi\sigma^*$ surfaces. Integrating the signal associated with the $^1\pi\sigma^*$ features in the derived TKER spectra, at a series

of Δt, subsequently allows a H^+ signal transient to be constructed. This transient can finally be analyzed *via* a kinetic fit to return a timescale, τ, which solely reflects the $^1\pi\sigma^*$ mediated AX–H fission dynamics.

In addition to the combined time and energy resolution gained by TR-VMI, image reconstruction methods also return a quantitative measure of the photofragment angular distributions, which can often be a critical tool for gleaning additional information about photodissociation processes [48] (note that this is not possible when using the magnetic-bottle analyzers mentioned above). Photoexcitation will preferentially excite molecules that have their electronic transition dipole moment ($\boldsymbol{\mu}$) aligned parallel to the electric field vector of the pump laser ($\boldsymbol{\varepsilon}$), where $\boldsymbol{\varepsilon}$ is parallel to plane of the position sensitive detector. For direct dissociation along $^1\pi\sigma^*$ states, which typically occurs on a timescale much faster than parent molecule rotation (see for example [20]), the angular recoil distribution of the photofragments will be preserved, and is related to the orientation of the dissociating bond coordinate with respect to $\boldsymbol{\mu}$. For a one-photon induced dissociation process, in the limit of axial recoil, the angular distribution of photofragments, $I(\theta)$, is given by the relationship [61]:

$$I(\theta) = \frac{\sigma}{4\pi}\left[1 + \frac{\beta_2}{2}\left(3\cos^2\theta - 1\right)\right] \tag{6.5}$$

where θ is the photofragment recoil angle with respect to $\boldsymbol{\varepsilon}$, σ is the photodissociation cross-section and β_2 is the anisotropy parameter. β_2 exhibits limiting values of -1 and $+2$ in cases where $\boldsymbol{\mu}$ lies orthogonal or parallel to the dissociating bond, respectively. Non-limiting negative and positive β_2 values can arises when $\boldsymbol{\mu}$ lies at an angle between $0°$ and $90°$ with respect to the bond fission coordinate, whereas $\beta_2 = 0$ corresponds to a purely isotropic photofragment recoil distribution. $\beta_2 = 0$ can arise through either: (i) $\boldsymbol{\mu}$ lying close to an angle of $54.7°$ to the bond fission coordinate; or (ii) dissociation taking place on a timescale significantly slower than the timeframe for rotational decoherence of excited parent molecules. In the case of rapid direct dissociation, the value of β_2 importantly allows one to extrapolate information regarding the initially excited electronic state, provided the orientation of $\boldsymbol{\mu}$ relative to the dissociating bond coordinate is known.

In Sect. 6.4 we move on to discuss examples where TR-MS and TR-VMI methods have been applied to understanding of $^1\pi\sigma^*$ mediated dynamics in a selection of heteroaromatic species, found as subunits in a variety of photostable biomolecules.

6.4 Applications

6.4.1 Non-adiabatic Versus Adiabatic Dynamics

Clocking ultrafast timescales for $^1\pi\sigma^*$ mediated H-atom elimination dynamics from an aromatic heterocycle was first reported by Radloff and co-workers using TR-MS [25]. This work focused on elucidating the timeframes for N–H bond fission
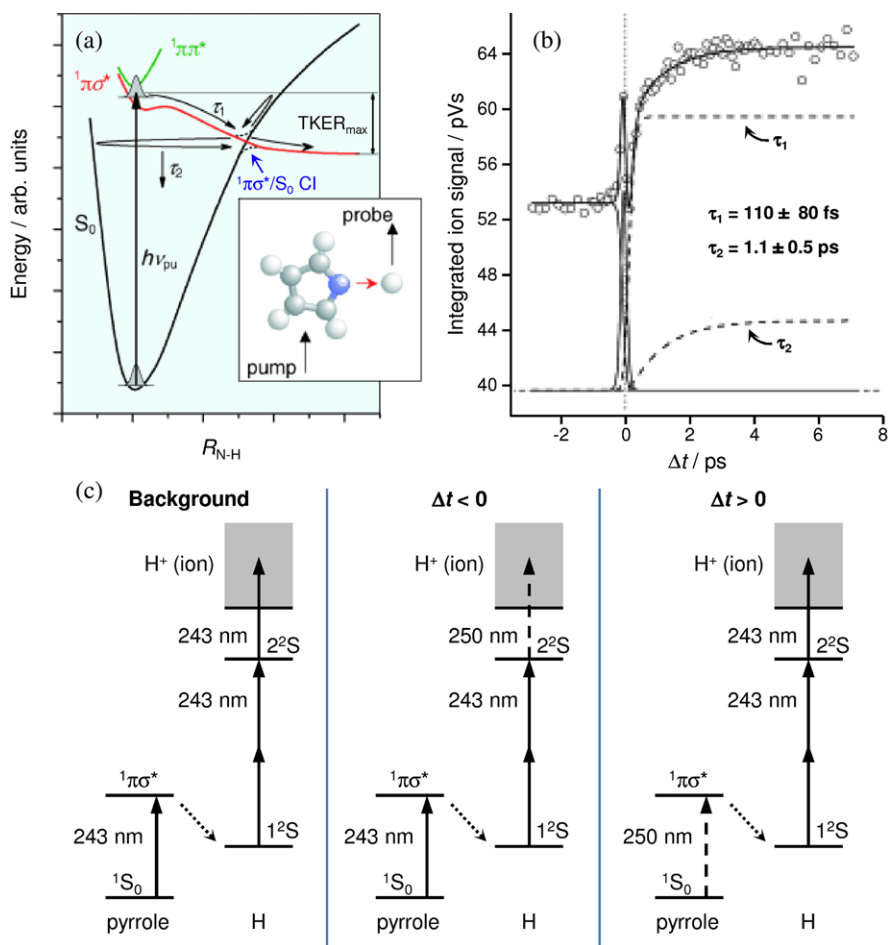
Fig. 6.5 (**a**) Schematic potential energy profiles of the S_0 ground state and lowest energy $^1\pi\pi^*$ and $^1\pi\sigma^*$ excited electronic states in pyrrole (molecular structure *inset*), with respect to the N–H bond coordinate (R_{N-H}). (**b**) Time-resolved H$^+$ signal transient (*open circles*) recorded from pyrrole using TR-MS with a 250 nm pump and 243 nm probe scheme. (**c**) Processes involved in the photolysis and ionization of H-atoms from pyrrole. Figure adapted from [25]

along the $^1\pi\sigma^*$ state in pyrrole (molecular structure shown in Fig. 6.5(a))—an aromatic subunit found in a variety of larger biomolecules, such as hemes. Figure 6.5(a) presents schematic potential energy profiles for the $S_0(^1A_1)$ ground state together with the first $^1\pi\pi^*(^1B_2)$ and $^1\pi\sigma^*(^1A_2)$ excited states in pyrrole, with respect to N–H bond length. Following excitation with a fs pump pulse centered at 250 nm, population is vibronically induced onto the $^1\pi\sigma^*$ state—a transition which is formally electric dipole forbidden in pyrrole's C_{2v} point group. This forbidden $^1\pi\sigma^*(^1A_2) \leftarrow S_0(^1A_1)$ transition gains oscillator strength by vibrational intensity borrowing from the higher lying $^1\pi\pi^*(^1B_2)$ manifold (or another higher energy

$^1\pi\pi^*$ state) [25, 62]. Using a temporally delayed fs probe pulse centered at 243 nm, the appearance timescale for any photodissociated H-atoms was subsequently monitored through $(2 + 1)$ REMPI, enabling the detection of H^+ with TR-MS. The results of these experiments are presented in Fig. 6.5(b). For all pump-probe delays, Δt, there is a constant (time-independent) one-color background signal, generated from the 243 nm probe *via* the process depicted in the left panel of Fig. 6.5(c). At $\Delta t < 0$ ps (*i.e.* pumping with 243 nm and probing with 250 nm), some H^+ signal is generated through an inefficient two-color 'probe-pump' process (Fig. 6.5(c), middle panel). At $\Delta t = 0$ ps delay, when the fs pump and probe pulses are temporally overlapped, a sharp spike in the H^+ signal is observed (due to a combination of multiphoton absorption processes [25]), which then decays within the temporal resolution of the experiment (~ 160 fs). Finally, when $\Delta t > 0$ ps, a notable rise in signal is observed, relative to negative pump-probe delays, correlating to the appearance of photodissociated H-atoms from pyrrole at 250 nm (Fig. 6.5(c), right panel). This signal rise exhibits a bi-exponential profile with two associated time constants, τ_1 and τ_2, which take values of 110 ± 80 fs and 1.1 ± 0.5 ps, respectively. With reference to Fig. 6.5(a), the ultrafast time constant, τ_1 (110 fs), is ascribed to the timescale for direct $^1\pi\sigma^*$ mediated N–H bond fission, proceeding *via* non-adiabatic passage through the $^1\pi\sigma^*/S_0$ CI, yielding H-atoms with large amounts of KE (defined by TKER$_{max}$) in coincidence with pyrrolyl (C_4H_4N) radical co-fragments in their electronic ground state. Alternatively, as population reaches the $^1\pi\sigma^*/S_0$ CI it may evolve adiabatically, traversing the upper cone of the CI and then returning to subsequently undergo non-adiabatic coupling back into vibrationally excited ground state species. Radloff and co-workers [25] postulated that the slower τ_2 time-constant (1.1 ps) originates from this initial adiabatic behavior around $^1\pi\sigma^*/S_0$ CI, resulting in statistical elimination of H-atoms with less KE from vibrationally hot S_0 species, after some degree of intramolecular vibrational energy redistribution (IVR) in S_0.

6.4.2 Comparing Dynamics in Simple Azoles

Upon exchanging one of the ring C–H bonds in pyrrole for an N atom, the simple azole isomers imidazole and pyrazole can be formed (structures shown in Fig. 6.6), both of which belong to the lower C_s symmetry group, transforming the $^1\pi\sigma^*(A'') \leftarrow S_0(A')$ transition into an electric dipole allowed process $(A' \otimes a'' \otimes A'' \supseteq A')$. Imidazole is a common subunit of photostable biomolecules, most notably in the amino acid histidine and the purine derived DNA bases adenine and guanine. In contrast, naturally occurring pyrazole derivatives are rare [64], particularly in biomolecules which are inherently required to be photostable. In light of this, TR-VMI experiments have begun to investigate whether there are any notable differences in the UV photochemistry of these two simple azole isomers [26], particularly along their $^1\pi\sigma^*$ states, despite their qualitatively similar electronic structure [63]—Fig. 6.6 presents schematic potential energy profiles along their N–H bond coordinates.
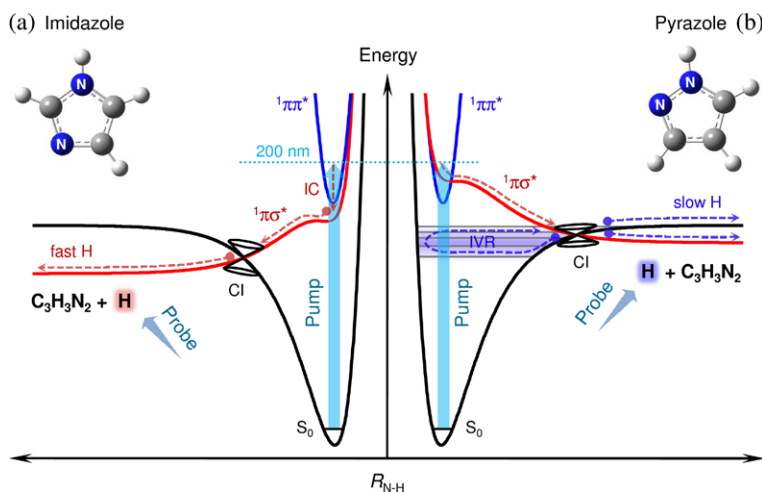
Fig. 6.6 Schematic potential energy profiles of the S_0 (*black*), $^1\pi\pi^*$ (*blue*) and $^1\pi\sigma^*$ (*red*) electronic states of (**a**) imidazole and (**b**) pyrazole (molecular structures *inset*) along their N–H bond coordinates (R_{N-H})—schematics are based on the calculated potentials in [63]. *Dashed red arrows* indicate rapid direct N–H bond fission *via* internal conversion (IC) through CIs onto the $^1\pi\sigma^*$ state, yielding high KE (fast) H-atoms. *Dashed blue lines* represent a possible pathway for IC back onto S_0 and statistical (slow) H-atom elimination following internal IVR on S_0. Figure adapted from [26]

H$^+$ velocity map images recorded following 200 nm excitation of imidazole and pyrazole, at delays of $\Delta t = 2.5$ and 600 ps, are shown contrasted as insets in Fig. 6.7(a) (top = 2.5 ps, bottom = 600 ps). Also presented are the TKER spectra derived from these images. The Gaussian-like features, centered at ~ 10000 cm^{-1} in both cases, correlate to probed H-atoms eliminated from the N–H bond along their $^1\pi\sigma^*$ states. In imidazole, excitation at 200 nm results in initial population of the $^1\pi\pi^*$ state, which can then couple through a CI (calculated to lie along an out-of-plane ring distortion coordinate [66]) onto the $^1\pi\sigma^*$ state, facilitating ultrafast N–H bond fission. The integrated H$^+$ signal transient for imidazole's $^1\pi\sigma^*$ signal feature (Fig. 6.7(b), left panel) reveals that this overall $^1\pi\pi^* \rightarrow^1 \pi\sigma^* \rightarrow$ N–H scission process occurs in 78 ± 40 fs [65], a timescale which has been further verified through complementary time-resolved photofragment translational spectroscopy measurements by Ullrich and co-workers [51]. In pyrazole, however, an analysis of the H$^+$ angular recoil distribution for the $^1\pi\sigma^*$ feature in the velocity map image ($\beta_2 = -0.5$) reveals that some fraction of population is directly imparted to the $^1\pi\sigma^*$ state upon UV excitation (albeit the weak one photon absorption cross-section for this transition) [57]. Figure 6.6(b) shows how pyrazole's $^1\pi\sigma^*$ state is (i) located higher in energy than the $^1\pi\pi^*$ state and (ii) is directly accessible at 200 nm [63]. As a result, direct population of the $^1\pi\sigma^*$ state at 200 nm in pyrazole delivers extremely rapid N–H bond cleavage, supported by the sub-50 fs time-constant extracted from the transient in the right panel of Fig. 6.7(b) [57].
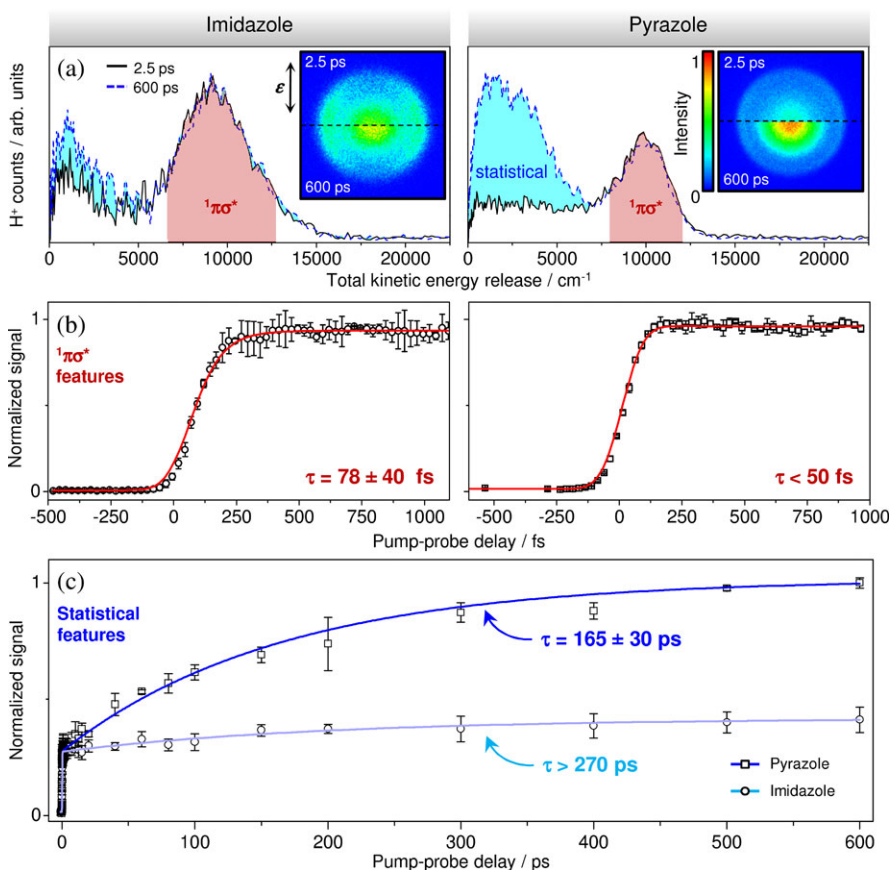
Fig. 6.7 (**a**) TKER spectra recorded at pump-probe delays of $\Delta t = 2.5$ and 600 ps for imidazole (*left*) and pyrazole (*right*). H^+ velocity map images from which the spectra are derived are provided *inset* (the *vertical arrow* indicates the electric field polarization of the pump laser, ε). (**b**) Integrated H^+ signal transients and kinetic fits (*red lines*) for the $^1\pi\sigma^*$ features in imidazole (*left*) and pyrazole (*right*). (**c**) Integrated H^+ signal transients and kinetic fits (*light blue* = imidazole, *dark blue* = pyrazole) for the 'statistical' features in imidazole and pyrazole. Figure adapted from [26, 57, 65]

In pyrrole, Radloff and co-workers considered the role of slower statistical H loss from vibrationally hot S_0 species after coupling back onto S_0 at the $^1\pi\sigma^*/S_0$ CI [25]. As discussed in Sect. 6.3.2, the TKER distribution of statistically ejected H-atoms exhibits a characteristic broad signal profile, peaked at low TKER [18, 59, 60]. One of the major advantages of the TR-VMI technique over TR-MS, is that the statistical H-atom signal component can be readily discerned from signal arising from direct $^1\pi\sigma^*$ driven dynamics, due to the simultaneous provision of both temporal and energetic information. This is aptly demonstrated in imidazole and pyrazole [26]. Upon increasing Δt to hundreds of picoseconds in imidazole, a minimal increase in signal at low TKER is observed (relative to the background

multiphoton signal observed at 2.5 ps [26, 65]), and is attributed to the onset of statistical H-atom elimination from hot S_0 species. This statistical feature appears with a time-constant of > 270 ps, shown by the transient in Fig. 6.7(c) (open circles). Selective deuteration of the N–H bond (N–D) also terminates any H$^+$ signal, revealing that H elimination in imidazole is localized to the N–H bond coordinate, even after coupling back onto S_0 [26]. In stark contrast, pyrazole exhibits a sizable gain in statistical H$^+$ counts by 600 ps, relative to imidazole (see Figs. 6.7(a) and (c)), and appears with a time-constant of $\tau = 165 \pm 30$ ps. Further measurements on deuterated isotopomers of pyrazole (either exclusive deuteration of all C–H bonds (C–D) or only the N–H bond (N–D)) reveals that there is change to $\sim 1{:}1$ ratio for statistical H loss from C–H:N–H coordinates in pyrazole [26] (unlike imidazole). It has been conjectured that irreversible photodamage of pyrazole through C–H bond fission and the generation of toxic free radicals may have played a role in the structural selectivity of imidazole over pyrazole in photostable biomolecules [26].

6.4.3 Excited State H-Atom Tunneling Dynamics

Over the years quantum tunneling of protons/hydrogen atoms has been implicated in a vast array of chemical [67] and biological [68] processes, such as photoacidity behavior [69, 70], alcohol dehydrogenase enzymes [71] and around the oxygen evolving complex site in photosystem II [72]. With respect to the latter, a series of proton-coupled electron-transfer reactions [73] are proposed to occur, one of which involves de-protonation of an O–H bond in a tyrosine residue *via* proton tunneling to a neighboring histidine acceptor site [72]. The residue of the amino acid tyrosine is the UV chromophore phenol, shown inset in Fig. 6.8. In recent years there has been a growing body of evidence to suggest that, over a specific UV excitation range (275–248 nm), photoexcited phenol itself exhibits a propensity for H-atom tunneling dynamics along the O–H coordinate under a $^1\pi\pi^*/^1\pi\sigma^*$ CI [27–29, 74]. It is this aspect of phenol's UV induced photochemistry which forms the topic of discussion for this section.

Calculated potential energy cuts along phenol's O–H bond coordinate by Ashfold and co-workers [28], shown in Fig. 6.8, serve to indicate how, after excitation to the zero point energy (ZPE) of the $^1\pi\pi^*$ state (275 nm), population may tunnel under the barrier formed by the $^1\pi\pi^*/^1\pi\sigma^*$ CI onto the $^1\pi\sigma^*$ state at elongated O–H bond lengths. This process subsequently gives rise to the elimination of high KE H-atoms, in coincidence with ground state phenoxyl radicals, $C_6H_5O(\tilde{X})$. Such a mechanism was first speculated in the theoretical work of Sobolewski *et al.* [14]. Later, experimental work by Pino *et al.* added further credence to this proposed tunneling mechanism [27]. This was achieved through TR-MS measurements, which compared the lifetimes extracted from parent cation signal decays following excitation to the $^1\pi\pi^*$ ZPE in a wide range of chemically substituted phenols and their hydrogen bonded complexes with NH$_3$. With the aid of complementary theory calculations, it was highlighted that phenol derivatives with a smaller vertical energy gap
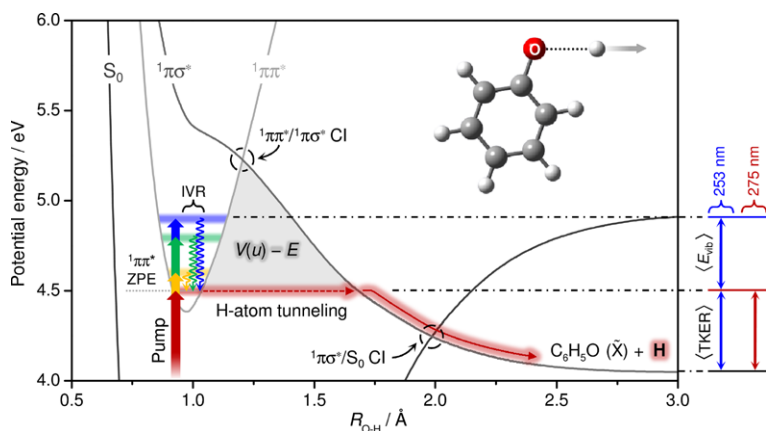
Fig. 6.8 Calculated potential energy cuts along the O–H bond coordinate (R_{O-H}) of phenol (molecular structure shown *inset*), obtained from reference [28]. Potentials were calculated at the CASPT2(10,10)/aug(O)-AVTZ level of theory. Excitation with fs pump pulses at 275 (*red*), 268 (*orange*), 258 (*green*) and 253 nm (*blue*) is indicated by the *vertical arrows*. *Wavy arrows* symbolize possible IVR back to the ZPE of the O–H stretch mode in $^1\pi\pi^*$ after excitation to modes orthogonal to the O–H stretch coordinate. The *grey shaded area*, labeled $V(u) - E$, highlights the barrier area used in 1-D BKW tunneling calculations. Figure adapted from [29]

between their $^1\pi\pi^*$ and $^1\pi\sigma^*$ states generally displayed reduced excited state lifetimes. Such an observation is in line with excited state decay dominated by tunneling under the $^1\pi\pi^*/^1\pi\sigma^*$ CI, as the excited state lifetime will be intimately linked to the size of the barrier area. Further support for this interpretation has since been garnered through frequency domain experiments, together with 2-D wavepacket calculations, by Dixon *et al.* [28], which imply that (on symmetry grounds) H tunneling is driven by the ν_{16a} mode (a ring torsion motion [75]) together with O–H stretching. Furthermore, fully deuterated phenol (C_6D_5OD) does not yield any signature of D-atom elimination *via* the $^1\pi\sigma^*$ state below the $^1\pi\pi^*/^1\pi\sigma^*$ CI [76], in line with the greatly reduced probability for D tunneling ($\sim 10^3$ times less than H [28]), allowing radiative decay processes to dominate and increase its fluorescence lifetime (~ 13 ns [77]).

Using TR-VMI, the dynamics of the excited state tunneling process in phenol can be tracked directly by monitoring the H-atom photoproducts [29]. A TKER spectrum recorded following excitation to the $^1\pi\pi^*$ ZPE at 275 nm in phenol is shown in Fig. 6.9(a) (derived from a H^+ velocity map image recorded at $\Delta t = 1.2$ ns). As with previously discussed examples, the dominant Gaussian feature centered at ~ 6000 cm^{-1} is assigned to O–H bond fission mediated by the $^1\pi\sigma^*$ state; the good accord between the predicted TKER$_{max}$ value for this process at 275 nm (Fig. 6.9(a), vertical red arrow) and the location of the Gaussian feature confirms this interpretation. As the pump energy is increased (268–253 nm), the center of the $^1\pi\sigma^*$ feature, highlighted as ⟨TKER⟩ in Fig. 6.9(a), remains in approximately the same location (only ~ 1000 cm^{-1} blue shift from 275–253 nm); this peak does, however, begin to broaden towards higher TKER, in agreement with the predicted increase in
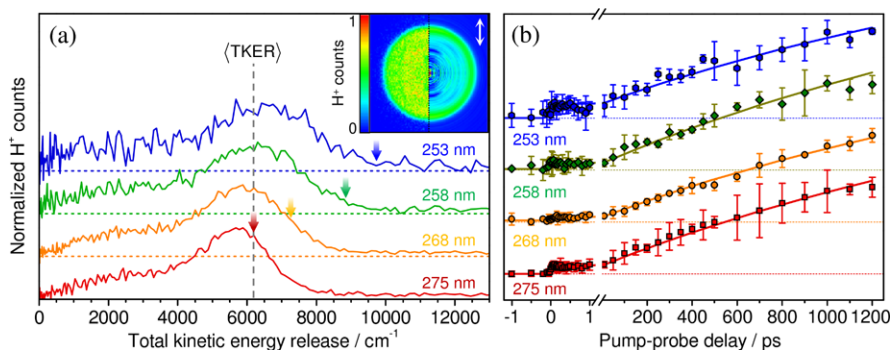
Fig. 6.9 (**a**) TKER spectra recorded following excitation with pump wavelengths centered at 275, 268, 258 and 253 nm in phenol. Spectra are recorded at a pump-probe delay of $\Delta t = 1.2$ ns. *Vertical arrows* indicate the predicted $TKER_{max}$ for O–H bond fission *via* the $^1\pi\sigma^*$ state at the given wavelengths (see (6.4)). An example H^+ image (275 nm pump) is shown *inset*, with the polarization of the pump laser, ε, indicated by the *white arrow* (*left* = raw image, *right* = deconvoluted slice). (**b**) Integrated H^+ signal transients for the $^1\pi\sigma^*$ features in phenol. *Solid lines* represent a kinetic model obtained from 1-D BKW tunneling calculations (6.6) using the calculated potential cuts in Fig. 6.8. Figure adapted from [29]

$TKER_{max}$ (Fig. 6.9(a), vertical arrows). With respect to the 1-D potential energy cuts along the O–H bond coordinate in Fig. 6.8, the minimal shift in $\langle TKER\rangle$ suggests that coupling onto $^1\pi\sigma^*$ below the $^1\pi\pi^*/^1\pi\sigma^*$ CI originates from (approximately) the same vibronic region of $^1\pi\pi^*$, irrespective of the initial excitation energy. Initially excited Franck-Condon active modes in $^1\pi\pi^*$, which are orthogonal to the O–H stretch coordinate (together with orthogonal modes populated following IVR), thus act as 'spectators' to the O–H fission process, mapping directly through into related modes (vibrational excitation) of the $C_6H_5O(\tilde{X})$ co-fragments [28]. This partitioning on the available energy between TKER and vibrational energy of the radical co-fragment, $\langle E_{vib}\rangle$, is schematically depicted on the right of Fig. 6.8 for 253 nm, relative to the scenario at 275 nm ($^1\pi\pi^*$ ZPE), where the majority of available energy is partitioned into TKER (N.B. even at 275 nm, frequency domain studies firmly indicate that $C_6H_5O(\tilde{X})$ is formed with a limited sub-set of vibrational modes, primarily an odd quanta progression of ν_{16a} in combination with ν_{18b} (an in-plane C–O wagging motion [28])). Within the context of the tunneling mechanism, the relative agreement between all $\langle TKER\rangle$ values and the predicted $TKER_{max}$ for O–H fission from the $^1\pi\pi^*$ ZPE, suggests that H tunneling always proceeds from around the ZPE of the O–H stretch in $^1\pi\pi^*$ [28], possibly populated following IVR (indicated by the wavy arrows in Fig. 6.8).

Figure 6.9(b) tracks the dynamics of the $^1\pi\sigma^*$ features at the four different pump wavelengths. It is apparent that: (i) H-atom elimination dynamics have not terminated by the temporal limits of the measurements (1.2 ns) for all pump energies; and (ii) there is no apparent increase in the rate of $^1\pi\sigma^*$ mediated H elimination as the pump energy increases (within the 1.2 ns temporal window of the experiments). The latter observation accords with exclusive tunneling from the ZPE of the O–H

stretch mode in $^1\pi\pi^*$; tunneling always proceeds through the same barrier area, irrespective of the initial pump energy. Using the calculated 1-D potential energy cuts in Fig. 6.8, together with the semi-classical Brillouin-Kramers-Wentzel (BKW) formalism [78], an (upper-limit) estimate of the tunneling lifetime, τ, from the ZPE of the O–H stretch in $^1\pi\pi^*$ can be determined according to:

$$\tau = \left[\nu_{\text{OH}} \exp\left(-2 \int_{u_1}^{u_2} \sqrt{\frac{2m}{\hbar^2}\big(V(u) - E\big)}\, du \right) \right]^{-1} \qquad (6.6)$$

where u is the O–H bond coordinate, ν_{OH} is the O–H stretch frequency (3581 cm^{-1} [79]), m is the mass of H, $V(u)$ is the potential barrier through which tunneling occurs (labeled on the potentials in Fig. 6.8) and E is the KE of the H-atom—defined as the ZPE of the O–H stretch in $^1\pi\pi^*$ (½ν_{OH}). This simple approach returns a value of $\tau = 2.5$ ns, in excellent agreement with an empirically derived value for τ (~ 2.4 ns [27]) as well as the measured fluorescence lifetime of the $^1\pi\pi^*$ ZPE level in phenol (~ 2.4 ns [77]). This predicted tunneling lifetime models all four H$^+$ signal transients in Fig. 6.9(b) (solid lines) and adds weight to the concept that the observed $^1\pi\sigma^*$ feature is born through tunneling onto $^1\pi\sigma^*$ from the ZPE of the O–H stretch mode in $^1\pi\pi^*$ at all excitation energies. Moreover, it also suggests that modes orthogonal to the O–H fission coordinate (with the exception of ν_{16a}—see [28]) have no major impact upon the effective tunneling rate. This specific picture of the excited state H-atom tunneling dynamics complements similar conclusions drawn from high resolution frequency domain measurements by Ashfold and coworkers [28], as well as more recent ultrafast time-resolved transient absorption studies of phenol dissociation in solution [74].

6.4.4 Competing $^1\pi\sigma^*$ Mediated Dissociation Pathways

As our understanding of $^1\pi\sigma^*$ dynamics in simple isolated heteroaromatics has expanded over the last decade, recent work has progressed to investigate the role of this behavior in more complex biologically relevant species [31–33, 81, 82]. In particular, there have been a small number of studies investigating competing dynamics along different $^1\pi\sigma^*$ surfaces within the same molecule. Notable subjects have included 4- and 5-hydroxyindole [83, 84], which contain both O–H and N–H bond coordinates, as well as $^1\pi\sigma^*$ driven H elimination along the amino (N^{10}H$_2$) and azole (N^{9}H) moieties in adenine [82]. Here, we use the model system mequinol (*para*–methoxyphenol, structure inset in Fig. 6.10) to discuss both the excitation energy dependence of competing dissociation channels, and the role of $^1\pi\sigma^*$ states localized along coordinates other than X–H bonds.

With respect to the schematic potentials shown in Fig. 6.10(a), we begin by considering H-atom elimination dynamics from the $^1\pi\sigma^*$ state located along mequinol's O–H coordinate ($^1\pi\sigma^*_{\text{O–H}}$). Note that mequinol can exist as either *trans* or *cis* rotamers (*trans* structure shown in Fig. 6.10), which are near-isoenergetic
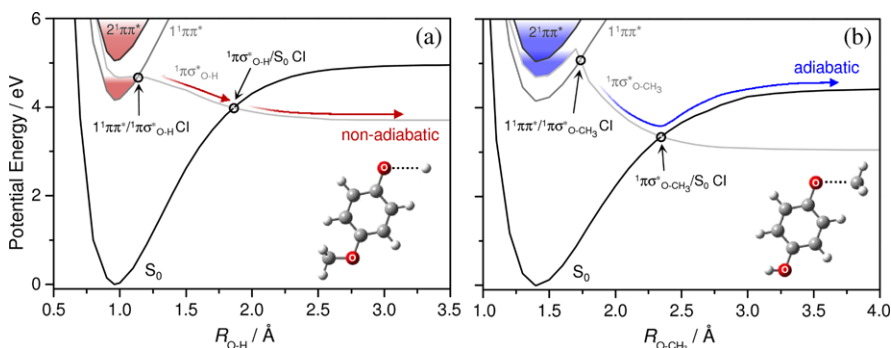
Fig. 6.10 Schematic 1-D potential energy cuts of the S_0, $1^1\pi\pi^*$, $^1\pi\sigma^*_{O-H}$ and $^1\pi\sigma^*_{O-CH_3}$ states along the (**a**) O–H (R_{O-H}) and (**b**) O–CH$_3$ (R_{O-CH_3}) bond coordinates of mequinol (molecular structure *inset*). The schematics are based on potentials calculated at the CASPT2(12,11)/aug-cc-pVTZ level [80]. *Shaded areas* of the potentials indicate excitation regions where subsequent $^1\pi\sigma^*_{O-H}$ (*red*) and $^1\pi\sigma^*_{O-CH_3}$ (*blue*) mediated dynamics are active. *Red arrows* indicate non-adiabatic dissociation dynamics while adiabatic dynamics are represented by *blue arrows*. Figure adapted from [80]

in S_0 ($\Delta E \sim 10$ cm^{-1} [80])—frequency-domain measurements, however, indicate that there is no significant difference in the $^1\pi\sigma^*$ governed dynamics of the two rotamers [80]. $^1\pi\sigma^*_{O-H}$ mediated H elimination in mequinol can be classified into two regimes: H tunneling (298–280 nm) and ultrafast dynamics ($\leq$ 245 nm), indicated by the red shaded regions in Fig. 6.10(a). Following excitation to the lowest energy $^1\pi\pi^*$ state ($1^1\pi\pi^*$) between 298 > λ > 280 nm, dynamics proceed through tunneling under the $1^1\pi\pi^*/^1\pi\sigma^*_{O-H}$ CI, in an analogous manner to phenol (see Sect. 6.4.3). The left panel in Fig. 6.11(a) displays a representative H$^+$ velocity map image (inset, $\Delta t = 1.2$ ns) and TKER spectra ($\Delta t = 1$ ps and 1.2 ns), in the H tunneling regime. The $^1\pi\sigma^*_{O-H}$ feature (centered at $\sim$ 5000 cm^{-1}) observed by 1.2 ns in the TKER spectrum correlates to H-atoms formed through non-adiabatic dissociation around the $^1\pi\sigma^*_{O-H}/S_0$ CI (Fig. 6.10(a), red arrows). A kinetic fit to this transient returns a H-atom appearance timescale of $\geq$ 1 ns, in qualitative agreement with an upper limit of the H tunneling lifetime obtained from calculated 1-D potentials using a simple BKW model ($\sim$ 10 ns [80]). Upon decreasing the excitation wavelength to 280 > λ > 245 nm no H-atom signal is observed at either low or high TKER. The origins of this are due to competition with O–CH$_3$ fission dynamics, which is discussed in more detail below. Decreasing the wavelength further ($\leq$ 245 nm) accesses the higher lying $2^1\pi\pi^*$ state, at which point coupling onto the $^1\pi\sigma^*_{O-H}$ state is reactivated (Fig. 6.11(b)). At these higher energies the $^1\pi\sigma^*_{O-H}$ feature shifts to higher TKER (centered at $\sim$ 10000 cm^{-1}) and is present by 1 ps, but remains correlated to non-adiabatic dissociation through the $^1\pi\sigma^*_{O-H}/S_0$ CI. A fit to the signal transient of this feature in Fig. 6.11(b) provides an ultrafast timescale of $\tau = 180 \pm 30$ fs for $^1\pi\sigma^*_{O-H}$ governed O–H scission, following initial excitation to $2^1\pi\pi^*$. In combination, these observations flag up a change in the mechanism for coupling onto the $^1\pi\sigma^*_{O-H}$ state, relative to the tunneling dynamics
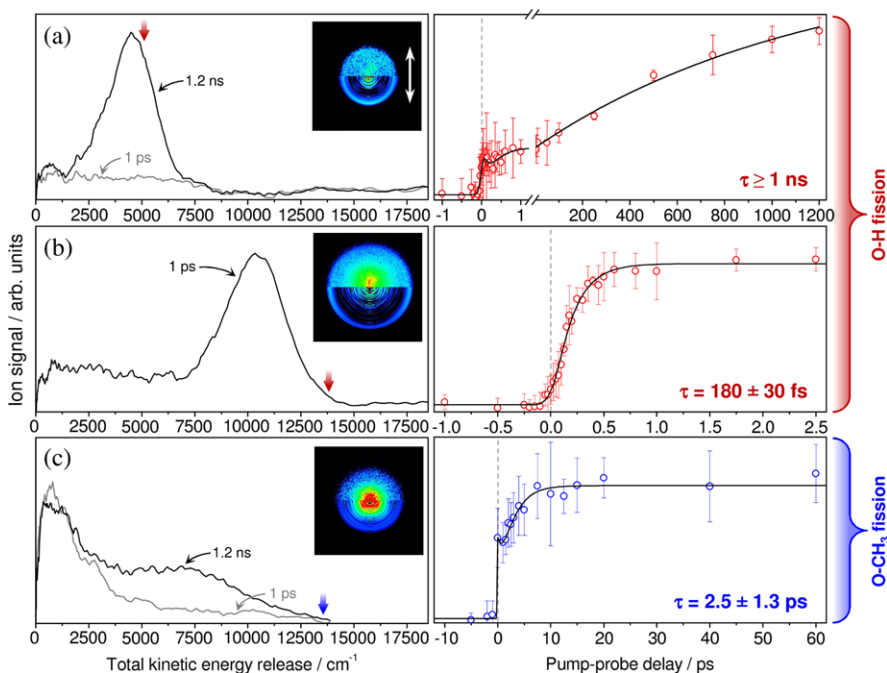
Fig. 6.11 Representative results from TR-VMI studies of O–H fission at (**a**) 298 nm and (**b**) 238 nm and O–CH$_3$ fission at (**c**) 238 nm in mequinol. The *left column* displays velocity map ion images ($\Delta t = 1.2$ ns) and time-resolved TKER spectra. *Vertical red arrows* indicate the predicted TKER$_{max}$ for non-adiabatic O–H fission, while the *vertical blue arrow* shows the predicted TKER$_{max}$ value for adiabatic O–CH$_3$ dissociation. The *right column* presents ion signal transients for the $^1\pi\sigma^*$ features. Figure adapted from [80]

at longer wavelengths. After initial excitation to $2^1\pi\pi^*$, population may either couple directly onto $^1\pi\sigma^*_{O-H}$ through a CI, or alternatively evolve through a series of $2^1\pi\pi^* \rightarrow 1^1\pi\pi^* \rightarrow {}^1\pi\sigma^*_{O-H}$ couplings. Once on $^1\pi\sigma^*_{O-H}$, transfer bond through the $1^1\pi\pi^*/^1\pi\sigma^*_{O-H}$ CI gives rise to non-adiabatic dissociation of the O–H bond through $^1\pi\sigma^*_{O-H}/S_0$ CI.

Recent research has demonstrated that $^1\pi\sigma^*$ dynamics are also active as a channel for CH$_3$ elimination, along X–CH$_3$ coordinates [85–88]. In mequinol there is a $^1\pi\sigma^*$ state localized along its O–CH$_3$ bond ($^1\pi\sigma^*_{O-CH_3}$) and electronic state potentials along this coordinate are shown in Fig. 6.10(b). Between 298–280 nm, no $^1\pi\sigma^*_{O-CH_3}$ mediated dynamics are observed. In this wavelength range excited state H tunneling dynamics dominate, whereas CH$_3$ tunneling under the $1^1\pi\pi^*/^1\pi\sigma^*_{O-CH_3}$ is not a kinetically competitive process due to the 15-times larger mass of CH$_3$. At wavelengths shorter than 280 nm however, dissociation along the $^1\pi\sigma^*_{O-CH_3}$ surface becomes an open channel, and representative findings from TR-VMI experiments (by REMPI probing CH$_3$ radical photoproducts at 333 nm [89, 90]) in this pump wavelength regime are displayed in Fig. 6.11(c). Inspection of the time-

resolved TKER spectra indicate that a $^1\pi\sigma^*_{O-CH_3}$ feature appears by 1.2 ns (centered at $\sim 7500\ \mathrm{cm}^{-1}$), although analysis of the energetics for O–CH$_3$ dissociation reveals that, unlike O–H fission along $^1\pi\sigma^*_{O-H}$, CH$_3$ elimination occurs adiabatically with respect to the $^1\pi\sigma^*_{O-CH_3}$/S$_0$ CI (TKER$_{max}$ for adiabatic O–CH$_3$ fission is indicated by the vertical blue arrow on the left panel of Fig. 6.11(c)). These adiabatic dynamics generate ground state CH$_3$ radicals in coincidence with *para*-hydroxyphenoxyl radicals in their first electronically excited state, HOC$_6$H$_4$O ($\tilde{A}$). This behavior has been tentatively attributed to a geometric phase effect around the $^1\pi\sigma^*_{O-CH_3}$/S$_0$ CI [80]—[91] provides a broader discussion on such phenomena.

Between $280 > \lambda > 245$ nm $^1\pi\sigma^*_{O-CH_3}$ driven O–CH$_3$ scission prevails over any H-atom elimination processes. Unlike the $^1\pi\sigma^*_{O-H}$ state, the potentials in Fig. 6.10(b) show that $^1\pi\sigma^*_{O-CH_3}$ exhibits a quasi-bound well in the vertical Franck-Condon region (~ 0.6 eV deep), which arises from strong mixing between a $^1\pi 3s$ Rydberg state (where the 3s orbital is associated with the O atom on the O–CH$_3$ coordinate) and the $^1\pi\sigma^*_{O-CH_3}$ valence state (reference [58] provides a general review of Rydberg-valence mixing). As a result, excitation between $280 > \lambda > 245$ nm induces population directly into the bound 3s Rydberg well of the $^1\pi\sigma^*_{O-CH_3}$ surface, localizing electron density onto the O–CH$_3$ moiety, and ultimately causes O–CH$_3$ fission to dominate over H elimination pathways. At $\lambda \leq 245$ nm, excitation to $2^1\pi\pi^*$ occurs and subsequent dynamics along both $^1\pi\sigma^*_{O-H}$ and $^1\pi\sigma^*_{O-CH_3}$ surfaces are active. However, the right panel in Fig. 6.11(c) highlights that O–CH$_3$ fission *via* $^1\pi\sigma^*_{O-CH_3}$ occurs on a timescale ($\tau = 2.5 \pm 1.3$ ps) an order of magnitude slower than O–H fission along $^1\pi\sigma^*_{O-H}$ at these excitation wavelengths, indicating that the initial coupling processes onto $^1\pi\sigma^*_{O-CH_3}$ and $^1\pi\sigma^*_{O-H}$ from $2^1\pi\pi^*$ must be kinetically competitive (both < 180 fs based on the timescale recorded for $^1\pi\sigma^*_{O-H}$ driven O–H fission). The timescale differences are thus attributed to the very different topographies of the two $^1\pi\sigma^*$ states; the purely dissociative profile of $^1\pi\sigma^*_{O-H}$ enables ultrafast elimination of H-atoms in a ballistic manner, whereas time is required for population to evolve out of the quasi-bound well on $^1\pi\sigma^*_{O-CH_3}$ and adiabatically advance towards electronically excited HOC$_6$H$_4$O ($\tilde{A}$) radicals, impeding O–CH$_3$ fission dynamics.

These detailed TR-VMI studies of mequinol, together with previous studies on hydroxyindoles [83, 84] and adenine [82], demonstrate the feasibility of untangling competing $^1\pi\sigma^*$ mediated dynamics in more complex heteroaromatic biomolecules. Future prospects include unraveling the role of competing $^1\pi\sigma^*$ dynamics in dihydroxyindoles (subunits of photostable biological eumelanin copolymers [92–94]) and DNA nucleosides.

6.4.5 Outlook

Developing a firmer understanding of $^1\pi\sigma^*$ mediated dynamics in photoexcited DNA bases, amino acids and their subunits provides the foundations for extending

this work to a plethora of more complex systems. One can envisage that future studies will entail working towards understanding the general role that this seemingly ubiquitous mechanism plays in the UV photochemistry of larger biomolecules. In particular, the tantalizing prospects of expanding this field to: (i) probe dynamics in species such as nucleosides and nucleotides in the gas phase; and (ii) investigate the dynamics of these bio-molecular building-blocks in solution, will invariably assist in cultivating such knowledge. Progress towards achieving both of these goals is currently underway. Techniques such as electrospray ionization [95–97], laser desorption [98–101] and laser-induced acoustic desorption [102], can provide the means to entrain large biomolecules into the gas phase and by-pass issues such as thermal decomposition. Likewise, experiments in solution are beginning to showcase the transference of knowledge attained from gas phase measurements; recent ultrafast studies on phenol [74] and *para*-methylthiophenol [74, 103] in the condensed phase reveal some distinct parallels with findings from the gas phase, even though the solvent can, in principle, manipulate $^1\pi\sigma^*$ mediated behavior. Furthermore, liquid microjets [104–106] offer significant potential for applying highly differential gas phase techniques (such as time-resolved photoelectron spectroscopy) to biomolecules in the condensed phase. These are fertile grounds for new and more expansive experiments, which will undoubtedly aid in constructing a more global picture of $^1\pi\sigma^*$ driven photochemistry in the molecular building-blocks of life.

References

1. V. Sundstrom, Annu. Rev. Phys. Chem. **59**, 53–77 (2008)
2. P. Kukura, D.W. McCamant, S. Yoon, D.B. Wandschneider, R.A. Mathies, Science **310**, 1006–1009 (2005)
3. M. Garavelli, D. Polli, P. Altoe, O. Weingart, K.M. Spillane, C. Manzoni, D. Brida, G. Tomasello, G. Orlandi, P. Kukura, R.A. Mathies, G. Cerullo, Nature **467**, 440–443 (2010)
4. G.D. Scholes, G.R. Fleming, A. Olaya-Castro, R. van Grondelle, Nat. Chem. **3**, 763–774 (2011)
5. S.R. Meech, Chem. Soc. Rev. **38**, 2922–2934 (2009)
6. I.R. Lee, W. Lee, A.H. Zewail, Proc. Natl. Acad. Sci. USA **103**, 258–262 (2006)
7. W.J. Schreier, T.E. Schrader, F.O. Koller, P. Gilch, C.E. Crespo-Hernandez, V.N. Swaminathan, T. Carell, W. Zinth, B. Kohler, Science **315**, 625–629 (2007)
8. G.P. Pfeifer, Y.H. You, A. Besaratinia, Mutat. Res. **571**, 19–31 (2005)
9. J. Li, Z.Y. Liu, C. Tan, X.M. Guo, L.J. Wang, A. Sancar, D.P. Zhong, Nature **466**, 887–890 (2010)
10. C.T. Middleton, K. de La Harpe, C. Su, Y.K. Law, C.E. Crespo-Hernandez, B. Kohler, Annu. Rev. Phys. Chem. **60**, 217–239 (2009)
11. C.E. Crespo-Hernandez, B. Cohen, P.M. Hare, B. Kohler, Chem. Rev. **104**, 1977–2019 (2004)
12. S. Ullrich, T. Schultz, M.Z. Zgierski, A. Stolow, Phys. Chem. Chem. Phys. **6**, 2796–2801 (2004)
13. M. Barbatti, A.J.A. Aquino, J.J. Szymczak, D. Nachtigallova, P. Hobza, H. Lischka, Proc. Natl. Acad. Sci. USA **107**, 21453–21458 (2010)
14. A.L. Sobolewski, W. Domcke, C. Dedonder-Lardeux, C. Jouvet, Phys. Chem. Chem. Phys. **4**, 1093–1100 (2002)
15. D.R. Yarkony, Rev. Mod. Phys. **68**, 985–1013 (1996)

16. W. Domcke, D.R. Yarkony, H. Koppel (eds.), *Conical Intersections: Theory, Computation and Experiment* (World Scientific, Singapore, 2011)
17. S. Matsika, P. Krause, Annu. Rev. Phys. Chem. **62**, 621–643 (2011)
18. M.N.R. Ashfold, G.A. King, D. Murdock, M.G.D. Nix, T.A.A. Oliver, A.G. Sage, Phys. Chem. Chem. Phys. **12**, 1218–1238 (2010)
19. M.L. Hause, Y.H. Yoon, A.S. Case, F.F. Crim, J. Chem. Phys. **128**, 104307 (2008)
20. A. Iqbal, M.S.Y. Cheung, M.G.D. Nix, V.G. Stavros, J. Phys. Chem. A **113**, 8157–8163 (2009)
21. C.P. Schick, P.M. Weber, J. Phys. Chem. A **105**, 3725–3734 (2001)
22. D.A. Blank, S.W. North, Y.T. Lee, Chem. Phys. **187**, 35–47 (1994)
23. J. Wei, A. Kuczmann, J. Riedel, F. Renth, F. Temps, Phys. Chem. Chem. Phys. **5**, 315–320 (2003)
24. G.A. King, T.A.A. Oliver, M.G.D. Nix, M.N.R. Ashfold, J. Phys. Chem. A **113**, 7984–7993 (2009)
25. H. Lippert, H.H. Ritze, I.V. Hertel, W. Radloff, ChemPhysChem **5**, 1423–1427 (2004)
26. G.M. Roberts, C.A. Williams, M.J. Paterson, S. Ullrich, V.G. Stavros, Chem. Sci. **3**, 1192–1199 (2012)
27. G.A. Pino, A.N. Oldani, E. Marceca, M. Fujii, S.I. Ishiuchi, M. Miyazaki, M. Broquier, C. Dedonder, C. Jouvet, J. Chem. Phys. **133**, 124313 (2010)
28. R.N. Dixon, T.A.A. Oliver, M.N.R. Ashfold, J. Chem. Phys. **134**, 194303 (2011)
29. G.M. Roberts, A.S. Chatterley, J.D. Young, V.G. Stavros, J. Phys. Chem. Lett. **3**, 348–352 (2012)
30. M.N.R. Ashfold, B. Cronin, A.L. Devine, R.N. Dixon, M.G.D. Nix, Science **312**, 1637–1640 (2006)
31. H. Satzger, D. Townsend, M.Z. Zgierski, S. Patchkovskii, S. Ullrich, A. Stolow, Proc. Natl. Acad. Sci. USA **103**, 10196–10201 (2006)
32. N.L. Evans, S. Ullrich, J. Phys. Chem. A **114**, 11225–11230 (2010)
33. A. Iqbal, V.G. Stavros, J. Phys. Chem. Lett. **1**, 2274–2278 (2010)
34. S.T. Tsai, C.K. Lin, Y.T. Lee, C.K. Ni, Rev. Sci. Instrum. **72**, 1963–1969 (2001)
35. C.M. Tseng, Y.T. Lee, M.F. Lin, C.K. Ni, S.Y. Liu, Y.P. Lee, Z.F. Xu, M.C. Lin, J. Phys. Chem. A **111**, 9463–9470 (2007)
36. X.M. Yang, Int. Rev. Phys. Chem. **24**, 37–98 (2005)
37. A.T.J.B. Eppink, D.H. Parker, Rev. Sci. Instrum. **68**, 3477–3484 (1997)
38. A. Stolow, A.E. Bragg, D.M. Neumark, Chem. Rev. **104**, 1719–1757 (2004)
39. R. Spesyvtsev, O.M. Kirkby, H.H. Fielding, Faraday Discuss. **157**, 165–179 (2012)
40. R. Montero, A.P. Conde, V. Ovejas, R. Martinez, F. Castano, A. Longarte, J. Chem. Phys. **135**, 054308 (2011)
41. R. Montero, A.P. Conde, V. Ovejas, F. Castano, A. Longarte, J. Phys. Chem. A **116**, 2698–2703 (2012)
42. D. Proch, T. Trickl, Rev. Sci. Instrum. **60**, 713–716 (1989)
43. U. Even, J. Jortner, D. Noy, N. Lavie, C. Cossart-Magos, J. Chem. Phys. **112**, 8068–8071 (2000)
44. W.C. Wiley, I.H. McLaren, Rev. Sci. Instrum. **26**, 1150–1157 (1955)
45. J.H. Moore, C.C. Davis, M.A. Coplan, *Building Scientific Apparatus*, 4th edn. (Cambridge University Press, Cambridge, 2009)
46. M. Nisoli, S. Desilvestri, V. Magni, O. Svelto, R. Danielius, A. Piskarskas, G. Valiulis, A. Varanavicius, Opt. Lett. **19**, 1973–1975 (1994)
47. D.W. Chandler, P.L. Houston, J. Chem. Phys. **87**, 1445–1447 (1987)
48. M.N.R. Ashfold, N.H. Nahler, A.J. Orr-Ewing, O.P.J. Vieuxmaire, R.L. Toomes, T.N. Kitsopoulos, I.A. Garcia, D.A. Chestakov, S.M. Wu, D.H. Parker, Phys. Chem. Chem. Phys. **8**, 26–53 (2006)
49. S.J. Cavanagh, S.T. Gibson, M.N. Gale, C.J. Dedman, E.H. Roberts, B.R. Lewis, Phys. Rev. A **76**, 052708 (2007)

50. N.L. Evans, H. Yu, G.M. Roberts, V.G. Stavros, S. Ullrich, Phys. Chem. Chem. Phys. **14**, 10401–10409 (2012)
51. H. Yu, N.L. Evans, V.G. Stavros, S. Ullrich, Phys. Chem. Chem. Phys. **14**, 6266–6272 (2012)
52. A.T.J.B. Eppink, S.M. Wu, B.J. Whitaker, in *Imaging in Molecular Dynamics: Technology and Applications*, ed. by B.J. Whitaker (Cambridge University Press, Cambridge, 2003), pp. 65–112
53. G.A. Garcia, L. Nahon, I. Powis, Rev. Sci. Instrum. **75**, 4989–4996 (2004)
54. G.M. Roberts, J.L. Nixon, J. Lecointre, E. Wrede, J.R.R. Verlet, Rev. Sci. Instrum. **80**, 053104 (2009)
55. P.M. Regan, S.R. Langford, A.J. Orr-Ewing, M.N.R. Ashfold, J. Chem. Phys. **110**, 281–288 (1999)
56. G.M. Roberts, C.A. Williams, J.D. Young, S. Ullrich, M.J. Paterson, V.G. Stavros, J. Am. Chem. Soc. **134**, 12578–12589 (2012)
57. C.A. Williams, G.M. Roberts, H. Yu, N.L. Evans, S. Ullrich, V.G. Stavros, J. Phys. Chem. A **116**, 2600–2609 (2012)
58. H. Reisler, A.I. Krylov, Int. Rev. Phys. Chem. **28**, 267–308 (2009)
59. R.H. Qadiri, E.J. Feltham, E.E.H. Cottrill, N. Taniguchi, M.N.R. Ashfold, J. Chem. Phys. **116**, 906–912 (2002)
60. E.J. Feltham, R.H. Qadiri, E.E.H. Cottrill, P.A. Cook, J.P. Cole, G.G. Balint-Kurti, M.N.R. Ashfold, J. Chem. Phys. **119**, 6017–6031 (2003)
61. R.N. Zare, *Angular Momentum: Understanding Spatial Aspects in Chemistry and Physics* (Wiley, New York, 1988)
62. B. Cronin, M.G.D. Nix, R.H. Qadiri, M.N.R. Ashfold, Phys. Chem. Chem. Phys. **6**, 5031–5041 (2004)
63. G.A. King, T.A.A. Oliver, M.G.D. Nix, M.N.R. Ashfold, J. Chem. Phys. **132**, 064305 (2010)
64. T. Eicher, S. Hauptmann, *The Chemistry of Heterocycles: Structure, Reactions, Syntheses, and Applications*, 2nd edn. (Wiley-VCH, Berlin, 2003)
65. D.J. Hadden, K.L. Wells, G.M. Roberts, L.T. Bergendahl, M.J. Paterson, V.G. Stavros, Phys. Chem. Chem. Phys. **13**, 10342–10349 (2011)
66. M. Barbatti, H. Lischka, S. Salzmann, C.M. Marian, J. Chem. Phys. **130**, 034305 (2009)
67. R.P. Bell, *The Tunnel Effect in Chemistry* (Chapman & Hall, London & New York, 1980)
68. A. Kohen, J.P. Klinman, Chem. Biol. **6**, R191–R198 (1999)
69. L.M. Tolbert, K.M. Solntsev, Acc. Chem. Res. **35**, 19–27 (2002)
70. J.T. Hynes, T.H. Tran-Thi, G. Granucci, J. Photochem. Photobiol. A, Chem. **154**, 3–11 (2002)
71. A. Kohen, R. Cannio, S. Bartolucci, J.P. Klinman, Nature **399**, 496–499 (1999)
72. S.Y. Reece, J.M. Hodgkiss, J. Stubbe, D.G. Nocera, Philos. Trans. R. Soc. Lond. B, Biol. Sci. **361**, 1351–1364 (2006)
73. R.I. Cukier, D.G. Nocera, Annu. Rev. Phys. Chem. **49**, 337–369 (1998)
74. Y. Zhang, T.A.A. Oliver, M.N.R. Ashfold, S.E. Bradforth, Faraday Discuss. **157**, 141–163 (2012)
75. M.N.R. Ashfold, A.L. Devine, R.N. Dixon, G.A. King, M.G.D. Nix, T.A.A. Oliver, Proc. Natl. Acad. Sci. USA **105**, 12701–12706 (2008)
76. M.G.D. Nix, A.L. Devine, B. Cronin, R.N. Dixon, M.N.R. Ashfold, J. Chem. Phys. **125**, 133318 (2006)
77. C. Ratzer, J. Kupper, D. Spangenberg, M. Schmitt, Chem. Phys. **283**, 153–169 (2002)
78. R.J. Le Roy, W.K. Liu, J. Chem. Phys. **69**, 3622–3631 (1978)
79. H.D. Bist, J.C.D. Brand, D.R. Williams, J. Mol. Spectrosc. **24**, 413–467 (1967)
80. D.J. Hadden, G.M. Roberts, T.N.V. Karsili, M.N.R. Ashfold, V.G. Stavros, Phys. Chem. Chem. Phys. **14**, 13415–13428 (2012)
81. M.G.D. Nix, A.L. Devine, B. Cronin, M.N.R. Ashfold, J. Chem. Phys. **126**, 124312 (2007)
82. K.L. Wells, D.J. Hadden, M.G.D. Nix, V.G. Stavros, J. Phys. Chem. Lett. **1**, 993–996 (2010)
83. T.A.A. Oliver, G.A. King, M.N.R. Ashfold, Phys. Chem. Chem. Phys. **13**, 14646–14662 (2011)

84. R. Livingstone, O. Schalk, A.E. Boguslavskiy, G.R. Wu, L.T. Bergendahl, A. Stolow, M.J. Paterson, D. Townsend, J. Chem. Phys. **135**, 194307 (2011)
85. A.G. Sage, M.G.D. Nix, M.N.R. Ashfold, Chem. Phys. **347**, 300–308 (2008)
86. C.M. Tseng, Y.T. Lee, C.K. Ni, J. Phys. Chem. A **113**, 3881–3885 (2009)
87. D.J. Hadden, C.A. Williams, G.M. Roberts, V.G. Stavros, Phys. Chem. Chem. Phys. **13**, 4494–4499 (2011)
88. J.S. Lim, S.K. Kim, Nat. Chem. **2**, 627–632 (2010)
89. J.W. Hudgens, T.G. Digiuseppe, M.C. Lin, J. Chem. Phys. **79**, 571–582 (1983)
90. R. de Nalda, J.G. Izquierdo, J. Dura, L. Banares, J. Chem. Phys. **126**, 021101 (2007)
91. S.C. Althorpe, in *Conical Intersections: Theory, Computation and Experiment*, ed. by W. Domcke, D.R. Yarkony, H. Koppel (World Scientific, Singapore, 2011), pp. 155–194
92. A.L. Sobolewski, W. Domcke, ChemPhysChem **8**, 756–762 (2007)
93. M. Gauden, A. Pezzella, L. Panzella, M.T. Neves-Petersen, E. Skovsen, S.B. Petersen, K.M. Mullen, A. Napolitano, M. d'Ischia, V. Sundstrom, J. Am. Chem. Soc. **130**, 17038–17043 (2008)
94. S. Olsen, J. Riesz, I. Mahadevan, A. Coutts, J.P. Bothma, B.J. Powell, R.H. McKenzie, S.C. Smith, P. Meredith, J. Am. Chem. Soc. **129**, 6672–6673 (2007)
95. J.B. Fenn, Angew. Chem., Int. Ed. Engl. **42**, 3871–3894 (2003)
96. J. Lecointre, G.M. Roberts, D.A. Horke, J.R.R. Verlet, J. Phys. Chem. A **114**, 11216–11224 (2010)
97. A.R. McKay, M.E. Sanz, C.R.S. Mooney, R.S. Minns, E.M. Gill, H.H. Fielding, Rev. Sci. Instrum. **81**, 123101 (2010)
98. E. Nir, K. Kleinermanns, M.S. de Vries, Nature **408**, 949–951 (2000)
99. M. Smits, C.A. de Lange, S. Ullrich, T. Schultz, M. Schmitt, J.G. Underwood, J.P. Shaffer, D.M. Rayner, A. Stolow, Rev. Sci. Instrum. **74**, 4812–4817 (2003)
100. A. Gahlmann, I.R. Lee, A.H. Zewail, Angew. Chem., Int. Ed. Engl. **49**, 6524–6527 (2010)
101. J. Zhou, O. Kostko, C. Nicolas, X.N. Tang, L. Belau, M.S. de Vries, M. Ahmed, J. Phys. Chem. A **113**, 4829–4832 (2009)
102. C.R. Calvert, L. Belshaw, M.J. Duffy, O. Kelly, R.B. King, A.G. Smyth, T.J. Kelly, J.T. Costello, D.J. Timson, W.A. Bryan, T. Kierspel, P. Rice, I.C.E. Turcu, C.M. Cacho, E. Springate, I.D. Williams, J.B. Greenwood, Phys. Chem. Chem. Phys. **14**, 6289–6297 (2012)
103. T.A.A. Oliver, Y. Zhang, M.N.R. Ashfold, S.E. Bradforth, Faraday Discuss. **150**, 439–458 (2011)
104. M. Faubel, K.R. Siefermann, Y. Liu, B. Abel, Acc. Chem. Res. **45**, 120–130 (2012)
105. C.P. Schwartz, J.S. Uejio, A.M. Duffin, A.H. England, D.N. Kelly, D. Prendergast, R.J. Saykally, Proc. Natl. Acad. Sci. USA **107**, 14008–14013 (2010)
106. P. Slavicek, B. Winter, M. Faubel, S.E. Bradforth, P. Jungwirth, J. Am. Chem. Soc. **131**, 6460–6467 (2009)